Oily water treatment by polyacrylonitrile/polysulfone blend ultrafiltration membrane embedded with alumina nanoparticles of improved antifouling properties

Maryam S. Karbol[1,2], Sama M. Al-Jubouri[1*]

[1] Department of Chemical Engineering, College of Engineering, University of Baghdad, Aljadria, Baghdad 10071, Iraq

[2] Department of Petroleum Engineering, College of Engineering, University of Karbala, Karbala, Iraq

* Email: sama.al-jubouri@coeng.uobaghdad.edu.iq, ORCID: 0000-0001-5080-411X

Abstract

The polyacrylonitrile (PAN)/polysulfone (PSF) blended polymer membranes were modified by decaethylene glycol monododecyl ether ($C_{12}EO_{10}$) as a non-ionic surfactant. Polymeric solutions containing 17 wt.% of both PAN and PSF with a ratio of 80/20, and $C_{12}EO_{10}$ with a mass concentration of 6 wt.% and aluminium oxide (Al_2O_3) nanoparticles with varying concentrations (1, 2, and 3 wt.%) were prepared. Adding 6 wt.% of $C_{12}EO_{10}$ to the casting solution formed a membrane with distinguished hydrophilicity and fouling resistance, higher porosity, appreciable permeate flux (77.1 L/m^2.h), and distinct vacuum gas oil rejection (92%) in comparison with the pure PAN ultrafiltration membrane. Further improvement for the PAN/PSF blend membrane using 2 wt.% of γ-Al_2O_3 in the presence of 6 wt.% of $C_{12}EO_{10}$ (PPCA-6-2γ membrane) produced an excellent permeate flux of 189.2 L/m²·h, favorable hydrophilicity with a contact angle of 26.55°, and an optimistic COD removal%, expressing the VGO rejection, of 97.15%. The PPCA-6-2γ membrane revealed acceptable separation performance up to four cycles of filtration and exhibited enhanced antifouling properties with an FRR% of 95.4%. The fouling mechanism that determines the flux reduction during crossflow ultrafiltration by the PPCA-6-2γ membrane was studied using the Hermia models. The cake layer formation model provided the best match for the experimental behavior when analyzing the flux reduction with time for the PPCA-6-2γ membrane. The fabrication cost was determined for PPCA-6-2γ membrane to be $1.67/20 g, respectively. So, the local manufacturing costs of the PPCA-6-2γ membrane did not surpass 90 $/m^2 of the membrane.

Keywords: Alumina nanoparticles; antifouling analysis; polyacrylonitrile/polysulfone blend membrane.

1. Introduction

Water scarcity is impacted by global industrial activities and population growth, requiring real solutions. One of the most important strategies to solve water pollution problems is water reuse, particularly in regions that would face water scarcity (Jain et al., 2023; Sadek and Al-Jubouri, 2023). Water pollution due to oil is a significant recent issue, as oily water comprises numerous contaminants, including heavy metals, oil and grease, and aromatic organic compounds. Wastewater by oil pollution adversely affects freshwater and marine resources due to the infiltration of contaminants into the ground, subsequently entering the ground and surface water (Sadek and Al-Jubouri, 2024). Furthermore, these contaminants hazard health of human (Ahmedzeki et al., 2009). Vacuum gas oil (VGO), often designated as heavy vacuum gas oil (HVGO), is a fuel derived from crude oil and frequently employed in maritime and automotive applications. The harmful effects of VGO encompass harm to aquatic ecosystems, threatening aquatic organisms, and soil degradation, resulting in crop losses. VGO poses numerous severe dangers to humans, including skin damage and cracking, as well as cancer.

Consequently, treating contaminated water became a serious demand. Several methods have been developed for oily water reclamation and potable water generation (Saraswathi et al., 2019). Membrane technology is a trustworthy option because of its excellent product quality, affordability, spatial efficiency, and ease of maintenance. Polymeric membranes are efficient for the exclusion of pollutants from surface water (Adday and Al-Jubouri, 2025; Koutahzadeh et al., 2018; Saraswathi et al., 2019). Utilization of cost-effective polymers may substantially decrease the total expenses associated with the membrane separation process (Ang et al., 2020; Etemadi et

al., 2020). Polyvinylidene fluoride and cellulose acetate are prevalent polymers utilized in water treatment. PAN is a commonly used polymer for membrane synthesis because it has advantages of cost-effectiveness, flexibility, excellent hydrophilicity, and low requirements for membrane formation conditions (Abedi et al., 2015; Zhao et al., 2012). Nevertheless, pure PAN-based membranes have several drawbacks, including low mechanical strength, poor chemical stability, and limited scope of applications (Hu et al., 2020). The PSF has good mechanical properties, excellent heat stability, and considerable resistance to alkali and biocompatibility (Zhao et al., 2015). However, the PSF has low water flux, hydrophobic properties, and anti-fouling ability, which makes it susceptible to dirt accumulation during use.

Polymer blending is a successful method for developing the characteristics of polymeric materials in a less complicated and cost-effective manner. The PAN/PSF blend membranes were synthesized, and they gave flux exceeding that of the pure PAN membrane (Ai-lian and Qing, 1995). Also, the hydrophilicity of PES/PAN blend membranes was investigated, and the membrane performance was enhanced at a specific blend of PES/PAN/PEG (Amirilargani et al., 2012). Previous investigations have demonstrated that the use of additives in the casting solutions of a membrane can modify the membrane's structure and reduce fouling. A polyoxyethylene (Brij 35) and polyethylene glycol dodecyl Ether (Brij-L4) showed successful results when added during the manufacturing of membranes because they act as pore-forming agents and increase the membrane hydrophilicity (Cortés et al., 2021; Wahab et al., 2019) . The additives' hydrophilicity also expedites the nonsolvent (water) inflow rate during membrane formation.

Emulsifiers and surfactants are generally amphiphilic compounds, possessing both hydrophilic polar and hydrophobic nonpolar regions. This chemical structure enables them to adhere to an interface and form a protective membrane around the dispersed phase. Emulsifiers or

surfactants are commonly categorized into anionic, cationic, non-ionic, and amphoteric types. Anionic surfactants have a negative charge, such as sodium dodecyl sulfate (SDS), and they are used in cleaning work, producing hygiene products, and emulsions (Sadek and Al-Jubouri, 2024). Cationic surfactants have a positive charge and dissociate in water into an amphiphilic cation and an anion. A large proportion of this class corresponds to nitrogen compounds such as fatty amine salts and quaternary ammoniums. Amphoteric surfactants have dual charges on their hydrophilic end, both positive and negative. The dual charges eliminate each other, resulting in a zero net charge, which is zwitterionic. Non-ionic surfactants that do not have any ions, like decaethylene glycol monododecyl ether ($C_{12}EO_{10}$), which can act as a pore-forming agent (Cerar et al., 2021). $C_{12}EO_{10}$ has a molecular weight of 626.86 g/mol, and its hydrophilic-lipophilic balance system equals 14.1. Thus, $C_{12}EO_{10}$ is considered a suitable hydrophilic additive (Karbol and Al-Jubouri, 2025).

Inorganic nanoparticles are also used to develop the properties of the polymeric matrix because it is a successful method of membrane modification (Mondal et al., 2024). The fabrication of mixed matrix membranes (MMMs), which consist of polymer-inorganic nanoparticle composites, offers a promising method for enhancing the separation, permeability, physicochemical characteristics, and antifouling characteristics of polymeric membranes (Ahmed et al., 2024; Kang and Cao, 2014). The integration of nanoparticles into membranes has garnered significant interest as an effective method to improve hydrophilicity. Diverse nanoparticles have been integrated into membranes, including silica, titanium dioxide, zeolite, lithium chloride, tin (IV) oxide, alumina, zirconium oxide, silver oxide, and zinc oxide. Alumina (Al_2O_3 NPs) may serve as a viable choice for the synthesis of the MMMs, due to their inorganic nature, excellent stability, low cost, and non-toxic characteristics (Ayaz et al., 2019). The incorporation of Al_2O_3

NPs in the PES membrane for eliminating copper ions from water was previously examined (Ghaemi, 2016). The PES-Al_2O_3 membrane demonstrated that the hydrophilicity and porosity of the membrane were enhanced by adding small amounts of Al_2O_3 NPs (≤1 wt.%) into the PES matrix, resulting in increased efficacy of repelling copper ions. The PSF-Al_2O_3 membrane for the exclusion of dyes from wastewater was fabricated (Kang and Cao, 2014). The results of this study indicated enhanced hydrophilicity, porosity, and antifouling properties of the PES membrane.

This research aims to improve the mechanical properties, hydrophilicity, and antifouling characteristics of the PAN/PSF blend membrane for the removal of VGO by embedding with Al_2O_3 NPs (gamma and alpha phases) at varying concentrations of 1, 2, and 3 wt.% in the presence of 6 wt.% of $C_{12}EO_{10}$. These membranes were developed for the first time for the treatment of oily water. The performance and morphology of these membranes were studied utilizing Fourier transform infrared spectroscopy, field emission scanning electron microscope, atomic Force Microscopy, and contact angle, and the results were compared with those of the pure PAN membrane. Furthermore, the regeneration, antifouling performance, fouling mechanism using the Hermia models, and the fabrication cost of the prepared membranes were investigated.

2. Experimental Work

2.1. Materials

PAN (Mwt 150,000 g/mol, the glass transition temperature (T_g) of 95 °C) was purchased from Sigma-Aldrich. PSF (Mwt 35,000 g/mol and T_g of 185 °C) was supplied by Shandong Natural Micron Pharm Tech CO., Ltd. N,N-Dimethylformamide (DMF) was supplied by Sigma-Aldrich (Germany). SDS was purchased from Thomas Baker Mumbai and used as an anionic surfactant. $C_{12}EO_{10}$ (HLB number of 14.1) was provided by Sigma-Aldrich and used as a non-ionic surfactant. Al_2O_3 NPs with gamma and alpha phases and an average size of 20 nm were obtained from

SkySpring (United States). Vacuum gas oil (VGO) as a model oil was provided by the Karbala Oil Refinery (Karbala, Iraq).

2.2. Preparation of Membranes

The pure PAN, PAN/PSF/$C_{12}EO_{10}$ (6wt.%), and PAN/PSF/Al_2O_3 membranes were fabricated via the non-solvent induced phase separation method. For the fabrication of the PAN/PSF blend membranes, the ratio was set at 80/20 based on the results of previous work (Karbol and Al-Jubouri, 2025). Also, the concentration of $C_{12}EO_{10}$ was set at 6 wt.% according to the results of that study. However, the MMMs were prepared by adding the Al_2O_3 NPs at different concentrations of 1, 2, and 3 wt.%. The Al_2O_3 NPs content in the prepared MMMs was chosen according to a published work (Etemadi and Qazvini, 2021). In all the synthesized membranes, the phase concentration of polymer, either pure or combined polymer, was 17 wt.%. Initially, Al_2O_3 NPs at a designated quantity were dispersed using sonication in the DMF solvent for 2 h to attain a uniform distribution. Then, the determined amount of the $C_{12}EO_{10}$ was added. Subsequently, the amounts of the PAN and PSF were added to the solvent-additive mixture and maintained at continual stirring for 24 h to achieve a homogenous combination. Following the degassing of the dope fluid, a casting solution layer membrane (200 μm) was cast onto a glass substrate. The glass board holding a cast layer was immersed in distilled water for 24 h to remove the residual solvent. Table 1 shows the materials composition used in the membrane preparation. The codes of the membranes shown in Table 1 were formed using the first letter of each material used in the preparation. The first P refers to PAN, the second P refers to PSF, C refers to $C_{12}EO_{10}$, and A refers to Al_2O_3 NPs. The first number in the code refers to the $C_{12}EO_{10}$ content, and the second number refers to the Al_2O_3 NPs content.

Table 1: The composition of materials used in membrane preparation.

Membrane ID	PAN (wt.%)	PSF (wt.%)	$C_{12}EO_{10}$ (wt.%)	α-Al_2O_3 (wt.%)	γ-Al_2O_3 (wt.%)	DMF (wt.%)
PAN	17	0	0	0	0	83
PAN/PSF/$C_{12}EO_{10}$ (6 wt.%)	13.6	3.4	6	0	0	77
PPCA-6-1α	13.6	3.4	6	1	0	76
PPCA-6-2α	13.6	3.4	6	2	0	75
PPCA-6-3α	13.6	3.4	6	3	0	74
PPCA-6-1γ	13.6	3.4	6	0	1	76
PPCA-6-2γ	13.6	3.4	6	0	2	75
PPCA-6-3γ	13.6	3.4	6	0	3	74

2.3. Characterization

To check the roughness parameters of the prepared membrane, atomic force microscopy (model AA3000, Angstrom Advanced Inc., USA) was used. Fourier-Transform Infrared spectroscopy (IRAffinity-1- SHIMADZU model) was used to study the surface chemistry of the membranes. The morphological characteristics of the synthesized membranes were investigated with field emission scanning electron microscopy (Tescan MIRA3 model). The energy dispersive spectroscopy analysis (ZEISS model, Germany) was utilized to provide the chemical composition of membranes. The mechanical properties of the prepared membranes were evaluated using tensile testing equipment (Tinius Olsen H50KT, USA). The contact angle of the synthesized membrane was determined by applying the probing liquid (distilled water) on the surface of the membrane using a T315A Picoliter dispenser to determine the hydrophilicity of the membrane.

The porosity of the membrane was determined using Equation 1 (Al-Maliki et al., 2023):

$$\varepsilon\ (\%) = \left(\frac{w_{wm} - w_{dm}}{A\ x\ l\ x\ \rho}\right) x100\% \quad (1)$$

Where: w_{wm} and w_{dm} are the weights of the wet and dry membranes, respectively, in g, A is the area of the membrane in cm^2, l is the thickness of the membrane in cm, and ρ is the density of water g/cm^3.

2.4. Examination of the filtration performance effectiveness and antifouling analysis

The flux (either PWF or J) of the prepared membranes was determined via a crossflow UF system using Equation 2 (Abbas and Al-Jubouri, 2025):

$$J = \frac{V}{A.t} \quad (2)$$

Where V (m^3) indicates the volume of the permeate flux, A (m^2) indicates the active area of a membrane, and t (h) indicates the permeation time.

The rejection of the VGO was assessed in the form of the rejection of the chemical oxygen demand (COD removal%) using Equation (3).

$$COD\ removal\ \% = \left(1 - \frac{COD_p}{COD_f}\right) x100 \quad (3)$$

Here, COD_p and COD_f are the COD concentrations in the permeate and feed (mg/L), respectively. The COD values were obtained via the COD reactor system MD200, Lovibond Model (Germany). Besides, the filtration performance of the developed membranes was examined at different VGO concentrations of 150-500 mg/L.

Following the flux (J_1) assessments, the flux of the VGO solution (J_{VGO}) was recorded at 90 min under transmembrane pressure (TMP) of 1 bar. After the separation of the VGO solution, the

contaminated membranes were cleansed with distilled water. Then, the water flux of the membranes (J_2) was recorded. The flux recovery ratio was analyzed to estimate the antifouling properties of the membranes using Equation 4 (Dasgupta et al., 2014):

$$FRR\ \% = \frac{J_2}{J_1} x\ 100 \quad (4)$$

Simultaneously, the reversible fouling ratio (R_{RF}%), irreversible fouling ratio (R_{IFR}%), and total fouling ratio (R_{TF}%) were estimated using Equations 5, 6, and 7, respectively (Saleem and Al-Jubouri, 2024):

$$R_{RF}\ \% = (\frac{J_2 - J_{VGO}}{J_1}) x\ 100 \quad (5)$$

$$R_{IFR}\% = (\frac{J_1 - J_2}{J_1}) x\ 100 \quad (6)$$

$$R_{TF}\% = RFR\ (\%) + \text{IFR}\ (\%) \quad (7)$$

3. Results and discussions

3.1. Fourier-transform infrared spectroscopy

The Fourier-transform infrared spectroscopy (FT-IR) results of pure PAN, PAN/PSF/$C_{12}EO_{10}$ (6wt.%), and PAN/PSF blend membranes modified by $C_{12}EO_{10}$ and Al_2O_3 NPs are illustrated in Figure 2. In the spectra of pure PAN membrane, the peak at 3350 cm^{-1} is associated with the O-H bonds. The characteristic peaks at 2985 cm^{-1}, 2431 cm^{-1}, and 1764 cm^{-1} are observed in the PAN membrane for the C-H groups, C≡N, and C=O bonds, respectively (Ruhland et al., 2017). For the PAN/PSF blend membrane, the peaks at 3431 cm^{-1}, 2924 cm^{-1}, 1726 cm^{-1}, and 1035 cm^{-1} can be assigned to O-H, C-H, C≡N, C=O, and C-O bonds, respectively (Etemadi et al., 2021). Figure 1 shows that the PPCA-6-2γ membrane has peaks at 3452 cm^{-1} and 3500 cm^{-1}, which might be attributed to the presence of the Al-OH bond in the Al_2O_3 NPs, which reinforces the O-H group.

The O-H group is more distinct and pronounced in the modified membranes than in the pure PAN and PAN/PSF/$C_{12}EO_{10}$ (6wt.%) membranes. The augmentation in the range and intensity of peaks in the presence of Al_2O_3 NPs indicates an improvement in the hydrophilicity of the membrane surface. The presence of the O-H group denotes that the membrane has good antifouling properties and hydrophilicity (Abdulsalam et al., 2020).

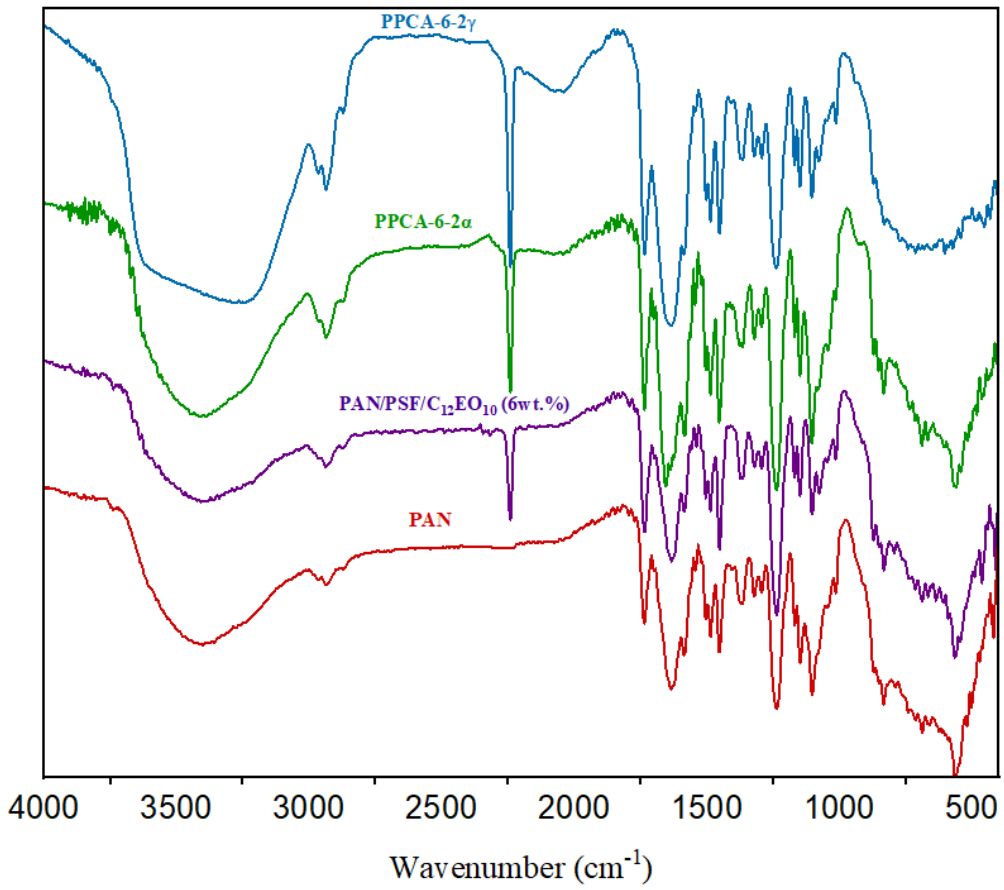

Figure 2: FT-IR analysis of PAN, PAN/PSF/$C_{12}EO_{10}$ (6wt.%), PPCA-6-2α, and PPCA-6-2γ membranes.

3.2. Field emission scanning electron microscopy

Figure 3 displays the field emission scanning electron microscopy (FE-SEM) images of the surface and the cross-section of the produced PAN, PAN/PSF/$C_{12}EO_{10}$ (6wt.%), PPCA-6-2γ, and PPCA-6-2α membranes. The pure PAN membrane texture contained fewer and shorter inner pores than

the PAN/PSF/$C_{12}EO_{10}$ (6wt.) membrane. Including $C_{12}EO_{10}$ in the PAN/PSF solution augmented the hydrophilic functional groups (O-H and C-H). $C_{12}EO_{10}$ expedited the exchange process between the DMF and distilled water. Figure 2B shows a coordinated, elongated, and broader finger-like structure with a dense skin layer extending from the top to the slender sponge layer in the PAN/PSF/$C_{12}EO_{10}$ (6wt.%) membrane, compared to the PAN membrane in Figure 2A.

The morphology of the membrane, shown in Figure 3 (C-D), drastically changed by adding nanoparticles, compared to pure PAN and PAN/PSF/$C_{12}EO_{10}$ (6wt.%) membranes shown in Figure 3 (A-B). As seen in Figure 3 (C-D), the upper layer displays a completely different structure depending on the phase of Al_2O_3 NPs added to the casting solution. The hydrophilic Al_2O_3 NPs caused an increase in thermodynamic instability in the casting solution and instantaneous demixing in the coagulation bath to form a more porous membrane structure. Therefore, very big macrovoids were formed in the structure of both PPCA-6-2γ and PPCA-6-2α membranes. Similar outcomes were reported in literature (Zhang et al., 2010).

3.3. Energy dispersive spectroscopy

The energy dispersive spectroscopy (EDX) analysis was conducted for the PPCA-6-2γ membrane to confirm the presence of γ-Al_2O_3 NPs in the membrane texture. EDX element mapping of the PPCA-6-2γ membrane shown in Figure 4 reveals that the chemical elements forming the Al_2O_3 (Al and O) are homogeneously distributed in the PPCA-6-2γ membrane. Also, the figure shows the composition of the PPCA-6-2γ membrane as follows: O was 93.5 wt.%, and Al was 6.5 wt.%. The high percentage of O is not only restricted by the presence of γ-Al_2O_3 NPs in the structure, as there are functional groups containing O that belong to PAN, PSF, and $C_{12}EO_{10}$.

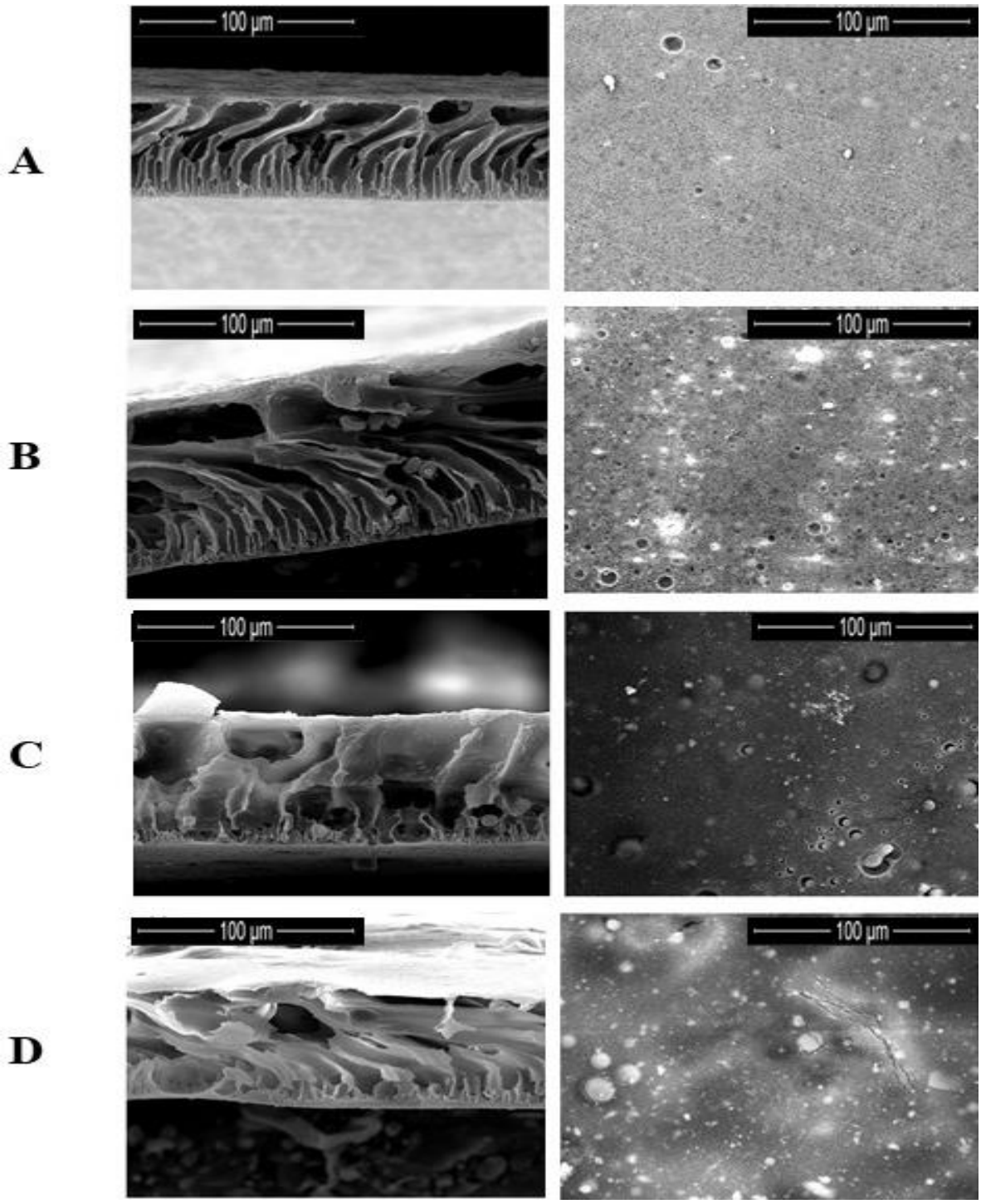

Figure 3: The FE-SEM images of the blend and modified membranes. The cross-section on the left side with a scale bar of 100 µm and the surface morphology on the right side with a scale bar of 100 µm. (A) pure PAN, (B) PAN/PSF/$C_{12}EO_{10}$ (6wt.%), (C) PPCA-6-2γ, and (D) PPCA-6-2α.

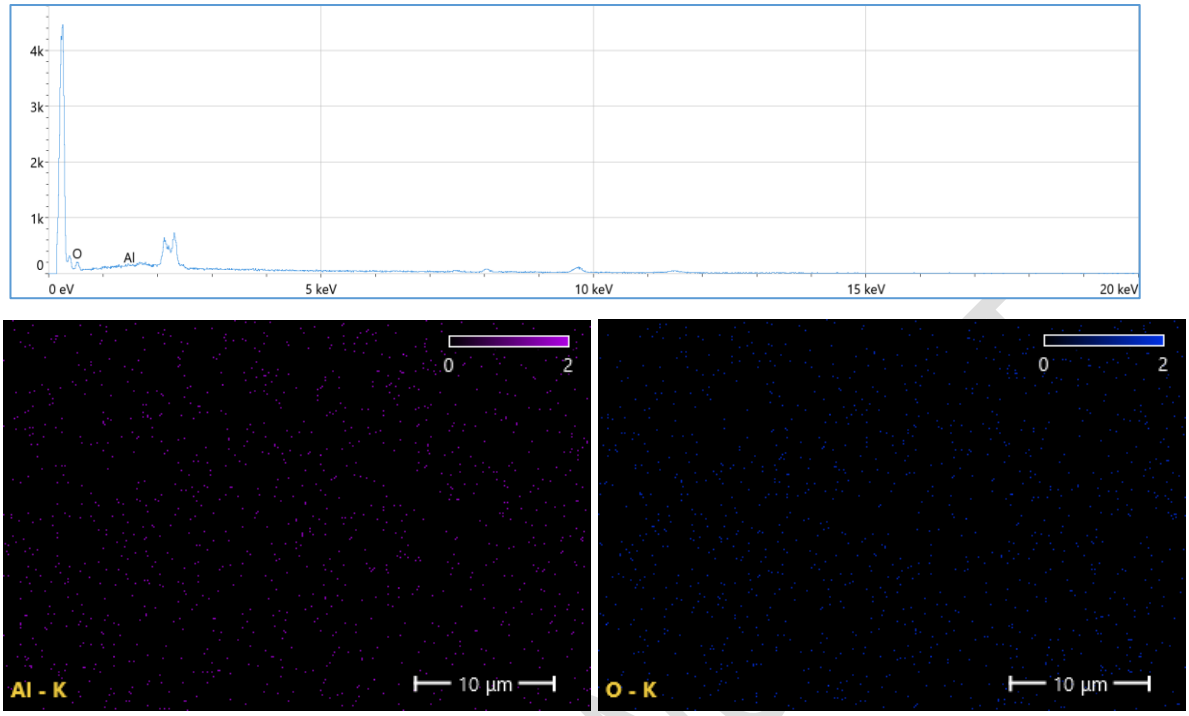

Figure 4: EDX analysis and element mapping of PPCA-6-2γ membrane.

3.4. Atomic Force Microscope analysis

Membrane roughness is a critical component influencing membrane fouling (Abdulameer and Al-Jubouri, 2022). Pollutants might accumulate in the valleys of the rough membrane surfaces, resulting in an increase in membrane fouling. Consequently, the fabrication of membranes with reduced roughness is crucial for the improvement of the final antifouling properties. The atomic force microscope (AFM) results of the PAN, PAN/PSF/$C_{12}EO_{10}$ (6wt.%), PPCA-6-2γ, as well as PPCA-6-2α membranes are shown in Figure 5, and the estimated surface roughness characteristics are displayed in Table 2. All developed membranes exhibited enhanced porosity in comparison to the pure PAN membrane. The augmentation of PAN porosity resulting from the integration of PSF material can be clarified as follows: the PSF is a glassy thermoplastic polymer characterized by a higher glass transition temperature (T_g) than PAN; hence, the incorporation of PSF into PAN resulted in a reduction of solution viscosity (Abdulsalam et al. 2020). The relationship between

porosity and viscosity is self-evident in the membrane preparation. The higher the polymer or additives concentration, the higher the solution's viscosity, which might decelerate phase separation and result in a more compact structure of the membrane with less porosity. However, additives like polyethylene glycol and polyvinylpyrrolidone might promote viscosity and produce a bigger pore size, enhancing porosity and permeability (Tan and Rodrigue, 2019). Table 2 shows that by adding PSF and $C_{12}E_{10}$, the pore size and surface roughness increased due to raising the viscosity and hydrophilicity of the dope solution. The viscosity of the casting solution has an important impact on the structure and pore size of the prepared membranes, as reported in another work (Tan et al., 2017) The surface of the PAN/PSF/$C_{12}EO_{10}$ (6wt.%) membrane in contrary of the PPCA-6-2γ and PPCA-6-2α membranes, showed higher roughness than the PAN membrane based on the roughness parameters represented by the root mean square height (R_q), arithmetic mean height or average roughness (R_a), and maximum height (R_z) shown in Table 2. These results agreed with those presented by previous work (Adday and Al-Jubouri 2025).

Table 2: The roughness parameters, porosity, and mean pore size of the prepared membranes.

Membranes	Roughness parameters			Porosity (%)	Mean pore size
	R_a (nm)	R_q (nm)	R_z (nm)		
PAN	87.25	119.54	702.13	48.01	29.75
PAN/PSF/$C_{12}EO_{10}$ (6wt.%)	314.1	230.5	1299	57.13	41.32
PPCA-6-2α	99.46	125.73	886.79	62.45	50.30
PPCA-6-2γ	83.29	102.67	624.85	66.70	56.13

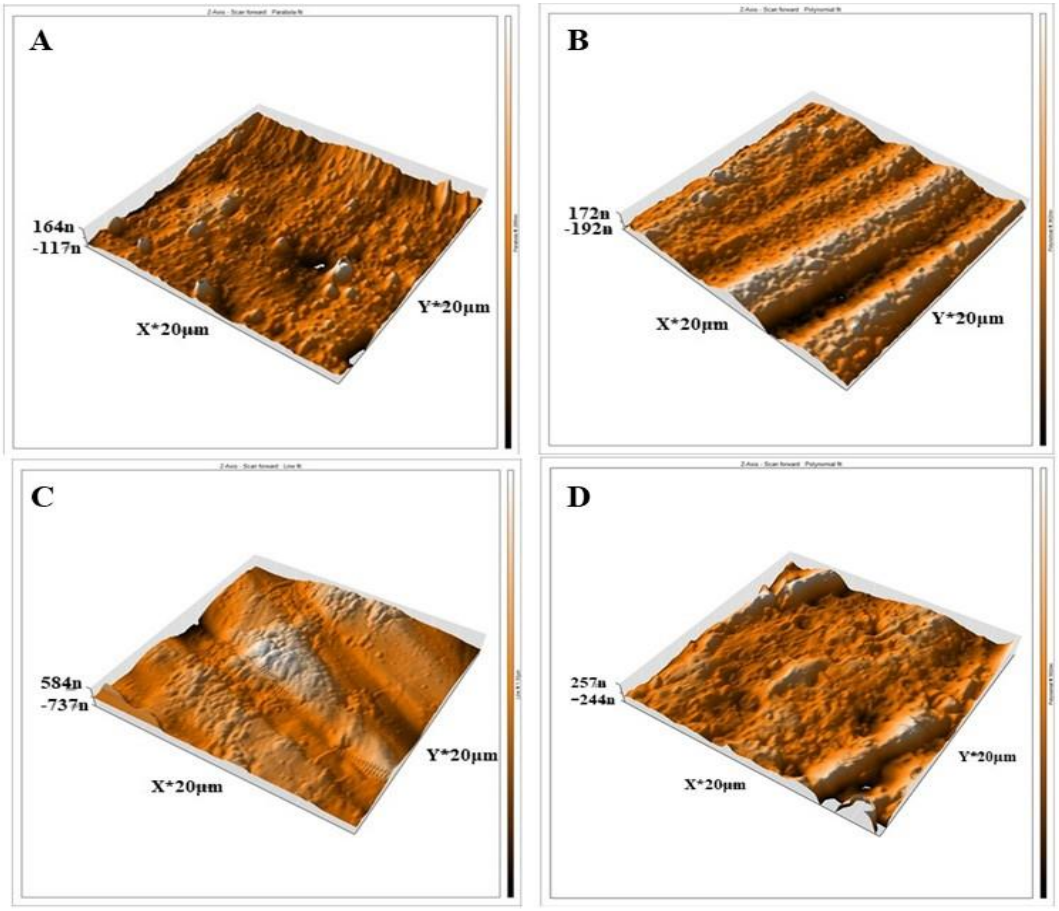

Figure 5: AFM images of the (A) Pure PAN, (B) PAN/PSF/$C_{12}EO_{10}$ (6wt.%), (C) PPCA-6-2γ and (D) PPCA-6-2α membranes.

3.5. Hydrophilicity and surface charge analysis

The effect of adding the $C_{12}EO_{10}$, α-Al_2O_3 NPs, and γ-Al_2O_3 NPs on the hydrophilicity of the prepared membranes was evaluated based on the values of the CA shown in Figure 6a. The PAN membrane showed the highest CA value of 63.01°. Adding 6 wt.% of water-soluble $C_{12}EO_{10}$ played a significant role in enhancing the membrane hydrophilicity, as the CA decreased to 31.14° for the PAN/PSF/$C_{12}EO_{10}$ (6wt.%) membrane. Also, the incorporation of Al_2O_3 NPs improved the surface hydrophilicity. The CA dropped to 29.63° and 26.55° for the PPCA-6-2α and PPCA-6-2γ

membranes, respectively. This characteristic is attributed to the increased surface hydrophilicity of the synthesized membranes by hydrophilic Al_2O_3 NPs, which increases the existence of hydrophilic groups on the membrane's surface, as shown by the FT-IR results displayed in Figure 1. These results concurred with those reported by another work (Ibrahim et al., 2020; Isloor et al., 2019).

The point of zero charge (pH_{PZC}) of the membrane is the point at which the net charge on the membrane surface is zero. The pH_{PZC} was calculated to show the effect of the pH on the membrane surface charge, as shown in Figure 6b. The PPCA-6-2γ membrane surface was negatively charged at pH above 6.3 and positively charged at pH below 6.3. The negative charge of the PPCA-6-2γ membrane was dominated because, during the manufacturing of the MMMs, many of the Al_2O_3 NPs were collected on the surface of the membrane, exposing O-H functional groups. The O-H group in a negatively charged membrane surface rapidly undergo protonation in the acidic aqueous solution, resulting in a positively charged surface (Tan et al., 2017).

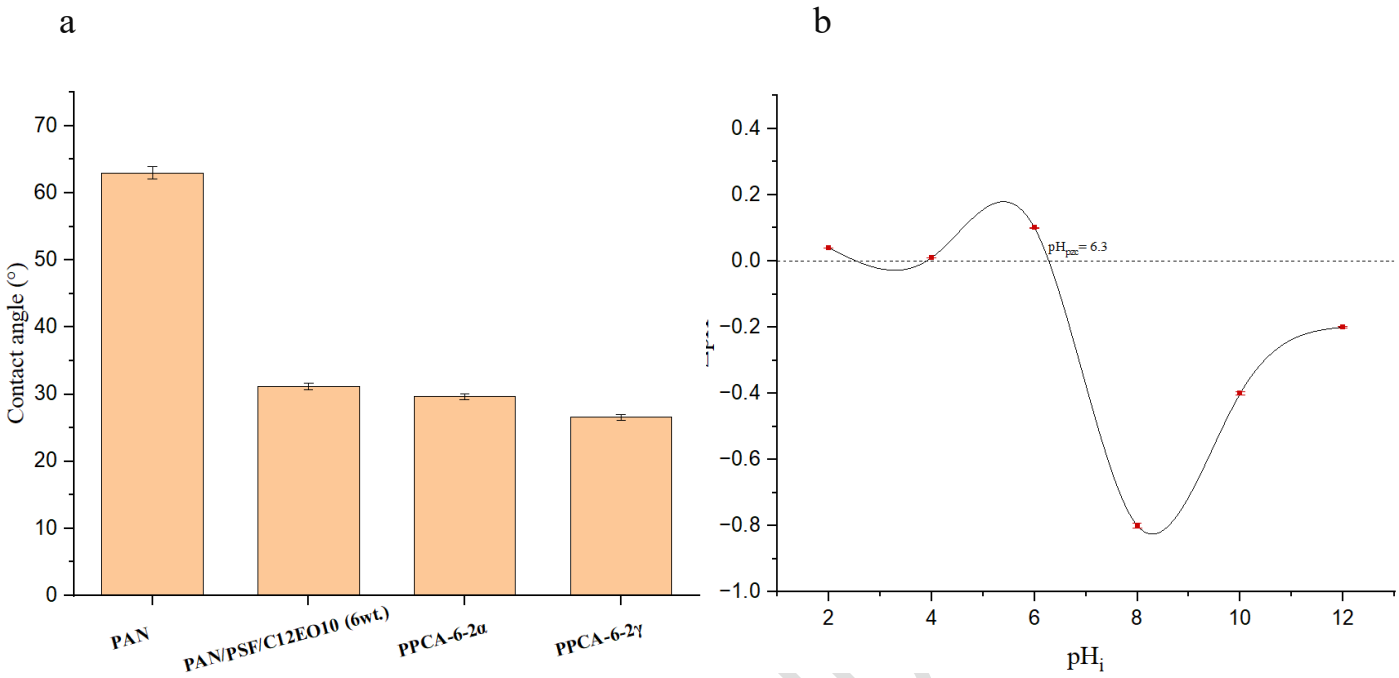

Figure 6: (a) Contact angle of the pristine and developed membranes and (b) pH_{PZC} of the PPCA-6-2γ membrane.

3.6. Mechanical properties

The tensile strength and elongation at break of the manufactured membranes were measured to assess their mechanical properties. Figure 7 shows that the tensile strength for the PAN membrane was 0.8 MPa because it has poor mechanical properties. Also, Figure 7 presents that the PAN/PSF/$C_{12}EO_{10}$ (6wt.%) membrane exhibited the maximum tensile strength of 4.8 MPa. This can be due to blending PAN with PSF, which has high mechanical strength and the introduction of 6 wt.% $C_{12}EO_{10}$, which increased the tensile strength and elongation of the polymer membranes. This result agreed with that reported in a published work (Liang et al., 2016). The addition of α-Al_2O_3 NPs raised the tensile strength to 5.7 MPa, and γ-Al_2O_3 NPs raised the tensile strength to 6.3 MPa for the PPCA-6-2α and PPCA-6-2γ membranes. In the same way, the Al_2O_3 NPs reinforced the membrane's structure to withstand load stress. The change in elongation was

moderate from 3.55% for the PAN membrane to 5.02%, 6.26%, and 6.34% for the PAN/PSF/$C_{12}EO_{10}$ (6wt.%), PPCA-6-2α, and PPCA-6-2γ, respectively.

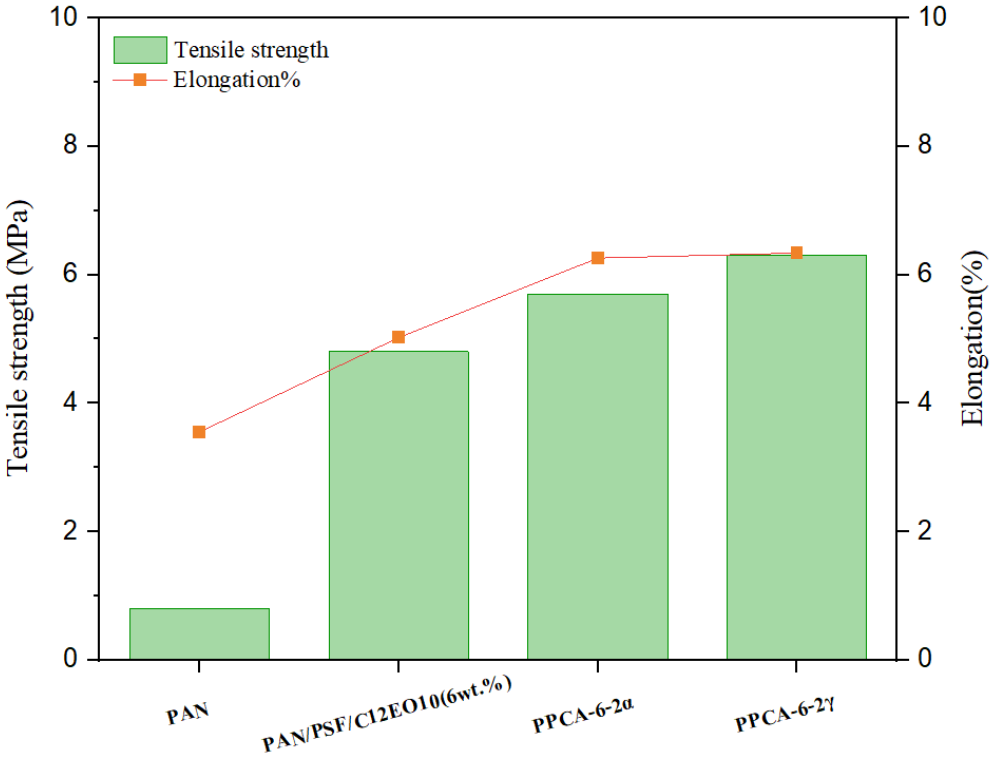

Figure 7: Mechanical properties of the prepared membranes.

3.7. Investigation of permeate flux and VGO removal of the prepared membranes

Figure 8 shows the permeate flux and COD removal for all developed membranes. Figure 8 displays that the permeate flux of the PAN membrane was 11.35 L/m².h. The permeate flux of the PAN membrane gradually increased in the presence of 6 wt.% $C_{12}EO_{10}$, which enhanced the porosity, which is an essential parameter for the permeation of water flux. All the MMMs exhibited improved permeate flux relative to PAN and PAN/PSF/$C_{12}EO_{10}$ (6wt.%) membranes. All the MMMs exhibited higher hydrophilicity and porosity compared to the PAN/PSF/$C_{12}EO_{10}$ (6wt.%) membranes (see Figure 6 and Table 2). Consequently, the permeate flux of the MMMs was

anticipated to rise. The highest permeate was obtained using PPCA-6-2γ. However, further increasing the γ-Al_2O_3 content to 3 wt.% gave reduced flux, which can be attributed to the reduced porosity and hydrophilicity raised by the accumulation of the Al_2O_3 NPs in the MMM structure. This result agreed with others in the literature (Abbas and Al-Jubouri, 2024; Nazemidashtarjandi et al., 2017; Zinadini et al., 2017).

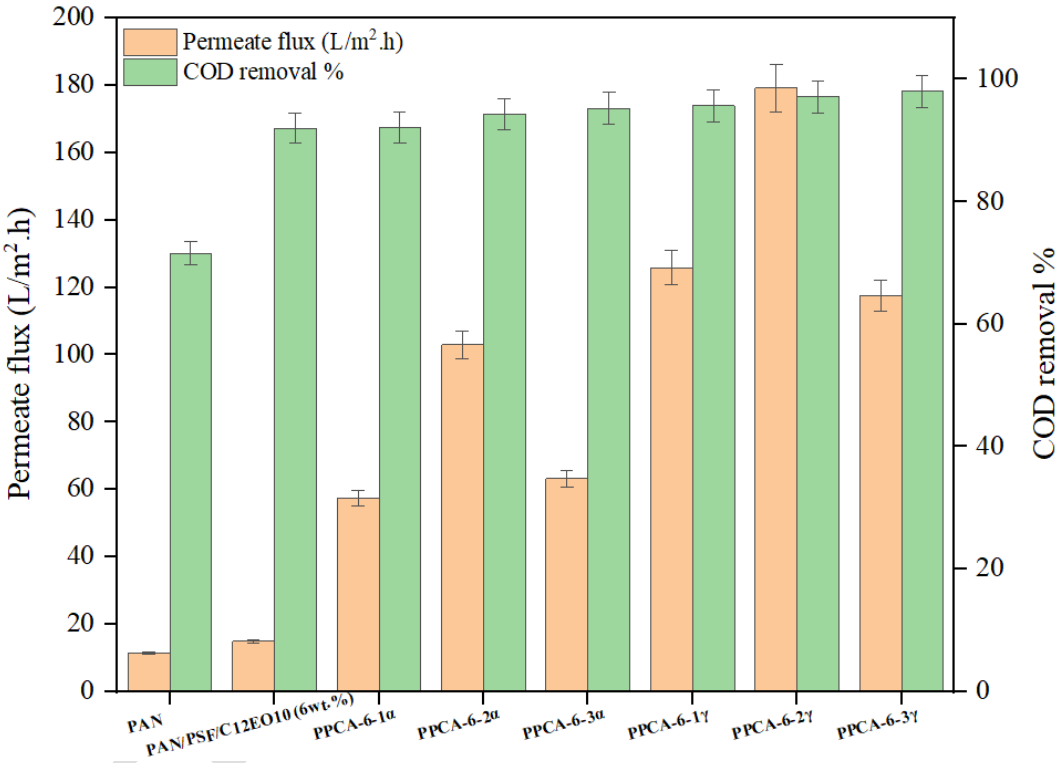

Figure 8: The permeate flux and COD removal% of prepared membranes.

The rejection of the VGO (COD removal%) for an initial VGO concentration of 150 mg/L was 72.6% for the PAN membrane, while the PAN/PSF/$C_{12}EO_{10}$ (6wt.%) membrane, which contained 6 wt.% of $C_{12}EO_{10}$, exhibited a VGO rejection of 92%, as shown in Figure 8. The inclusion of Al_2O_3 NPs increased the COD removal% to 94.32% and 97.15% for the PPCA-6-2α and PPCA-6-2γ membranes, respectively. The reduction of the permeate flux and the elevation of

COD removal% with rising concentration of Al_2O_3 NPs can be attributed to the aggregation of the nanoparticles on the membrane surface during the casting process. The accumulation of nanoparticles on the membrane surface increased the thickness of the active layer, resulting in decreased porosity and hydrophilicity. The result is consistent with those reported in a published work (Hosseini et al., 2020).

3.8. Effect of the initial VGO concentration

Figure 9 displays the impact of initial VGO concentrations (150, 250, and 500 mg/L) on the permeate flux and COD removal% of the PPCA-6-2γ membrane. The permeate flux marginally diminished with raising the initial VGO concentration. The flux decreased from 189.2 to 112.3 and 97.18 $L/m^2.h$ at concentrations of 150, 250, and 500 mg/L, respectively. A high VGO concentration created a cake layer on the membrane surface, hence decreasing the flux. The COD removal% significantly declined from 97.15% to 79.26% and 63.48% at concentrations of 150, 250, and 500 mg/L, respectively, due to the increased deposition of oil droplets on the membrane surface. The occurrence of the concentration polarization phenomenon at high VGO concentrations led to the transportation of oil molecules from the membrane to the permeate side, hence reducing the membrane's efficacy in retaining oil.

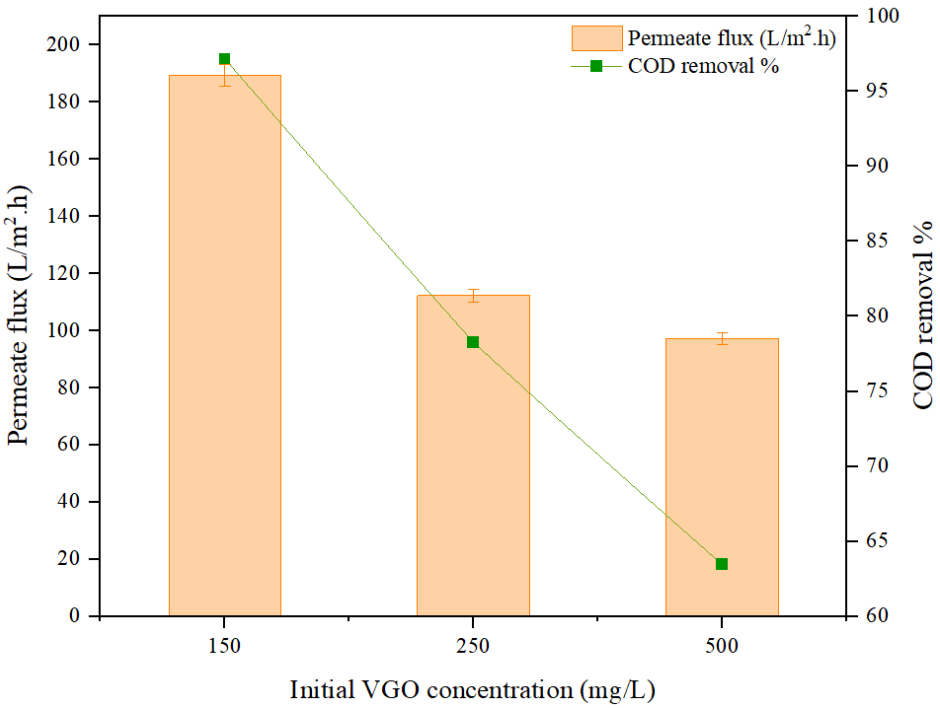

Figure 9: Effect of the initial VGO concentration on the separation performance of the PPCA-6-2γ membrane.

3.9. Antifouling study

To examine the antifouling properties of the synthesized membranes used for the VGO separation, the fouling parameters R_{FR}%, R_{IFR}%, R_{TF}%, and FRR% were assessed for each cycle using these membranes, as depicted in Figure 10. Typically, R_{IFR}% is caused by sharp interactions between foulants and the surface pores of the membrane (Saleem et al., 2025; Vatanpour et al., 2012). The pristine PAN membrane exhibited an R_{IFR}% of 42.16%; however, this value diminished to 31% for the PAN/PSF/$C_{12}EO_{10}$ (6wt.%) membrane and to 19.7% for the MMMs at 2 wt.% of γ-Al_2O_3 NPs. The R_{IFR}% value decreased due to the low roughness of the PAN/PSF/$C_{12}EO_{10}$ (6wt.%) membrane and MMMs compared to the pure PAN membrane. Rougher membranes possess more foulant attachment sites, thereby increasing fouling (Abdikheibari et al., 2018). Furthermore, enhanced membrane hydrophilicity limited the adsorption of hydrophobic foulants

on the membrane surface (Karimi et al., 2020). Figure 10a shows that the MMMs had a reduced R_{IFR}% relative to other samples, due to their enhanced hydrophilicity. Figure 10a shows that the FRR% of the PAN/PSF/$C_{12}EO_{10}$ (6wt.%) membrane and MMMs exceeded that of the pristine PAN membrane. The FRR% was 77.5% for the pure PAN membrane, but it increased to 88.9%, 90.72%, and 95.4% for the PAN/PSF/$C_{12}EO_{10}$ (6wt.%), PPCA-6-2α, and PPCA-6-2γ, respectively. Reducing the membrane surface roughness diminished fouling of the produced membranes, leading to an increase in FRR% (Sadek and Al-Jubouri, 2024). Figure 10 shows that the addition of nanoparticles to the membrane casting solution increased FRR% due to its low roughness and enhanced hydrophilicity.

The recyclability test assesses the membrane's stability and durability to guarantee its prolonged functionality. The PPCA-6-2γ membrane was examined in four cycles of VGO filtration, each cycle lasting for 1 h, followed by a 30 min cleaning procedure utilizing a 5 mM SDS solution at 45 ºC. Figure 10b displays the findings of the reusability examination. In the fourth cycle, the FRR% for the PPCA-6-2γ membrane decreased to 60.1%. The reduction in FRR% resulted from a surfactant layer enclosing small oil droplets that coalesce to create bigger oil droplets, as reported in (Khader et al., 2025). The oil droplets spread over the membrane's surface, reducing interaction between water and the membrane's surface. While the cleaning procedure may not entirely restore the membrane's surface performance, the γ-Al_2O_3 NPs demonstrated exceptional antifouling efficacy for the modified PPCA-6-2γ membrane.

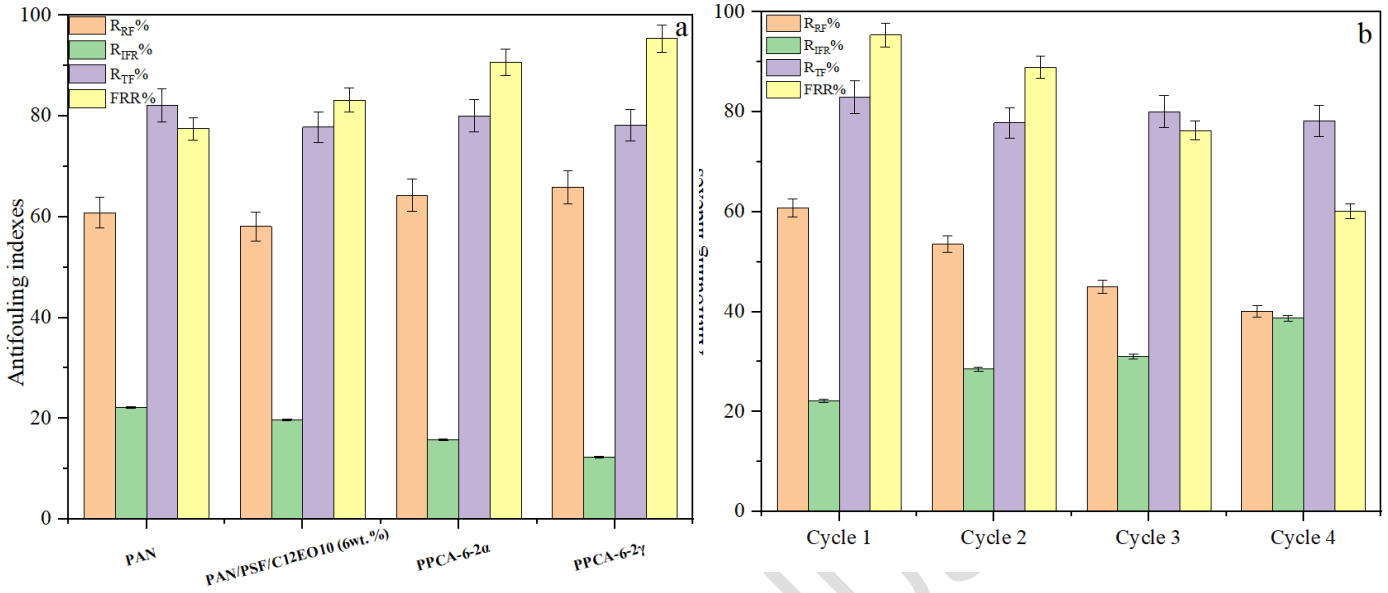

Figure 10: (a) Antifouling parameters for membranes in the filtration of VGO and (b) Antifouling analysis of the cycles of the PPCA-6-2γ membrane.

3.10. Fouling Models

Hermia's fouling models were applied to the data obtained from studying the VGO filtration to determine the fouling mechanism of the PPCA-6-2γ membrane. The fouling mechanisms can be categorized into four types: complete pore blocking, intermediate pore blocking, standard pore blocking, and cake layer formation. In complete pore blocking, the particles are of equal size to the pores of the membrane, which completely block the entrances and prevent the flow. Hermia developed a general equation which can be used for all types of fouling, depending on the value of n, as shown in Equation 8

$$\frac{d^2t}{dv^2} = K\left(\frac{dt}{dv}\right)^n \qquad (8)$$

The fouling type depends on the magnitude of n present in Equation 8. For complete pore blocking, n = 2. Hermia's model of the complete pore blocking mechanism in crossflow is shown by Equation 9 (Sadek et al., 2024).

$$\ln\left(\frac{1}{J_{VGO}}\right) = K_B t + \ln\left(\frac{1}{J_0}\right) \quad (9)$$

Where K_B is the coefficient of complete pore blocking (m^2/L)

Standard pore blocking results in a decrease in porosity of the membrane and an increase in the membrane resistance because of the ability of tiny particles to adhere to the inner wall of the pores, constricting them and minimize the flow rate. Hermia's model of the standard pore blocking mechanism in crossflow is shown by Equation 10 (Saleem et al., 2025). For this model, the n value shown in Equation 8 is 3/2.

$$\frac{1}{(J_{VGO})^{0.5}} = K_S t + \frac{1}{(J_0)^{0.5}} \quad (10)$$

Where K_S is the coefficient of standard pore blocking ($m/L^{0.5}.min^{0.5}$).

In the intermediate pore blocking, there is an accumulation of some particulates at the top of already precipitated particulates, plugging the pore openings. Hermia's model of the intermediate pore blocking mechanism, as shown in Equation 11 (Iritani and Katagiri, 2016). For this model, the n value shown in Equation 8 is 1.

$$\frac{1}{J_{VGO}} = K_i t + \frac{1}{J_0} \quad (11)$$

Where K_i is the coefficient of intermediate pore blocking (m^2/L).

Formation of cake layers is a process in which large particles accumulate on the surface of a membrane, forming a permeable cake that is not completely impermeable. Hermia found the

mathematical properties of the cake formation with a special case of constant filtration pressure as shown in Equation 12. For the cake layer formation, the value of n shown in Equation 8 is 0.

$$\frac{1}{(J_{VGO})^2} = K_C t + \frac{1}{(J_0)^2} \quad (12)$$

Where K_C is the coefficient of cake layer formation ($m^4.min/L^2$).

Figure 11 and Figure 12 show the plots of Hermia's models. Table 3 displays the values of the fitting parameters and equations of the first and third cycles for the PPCA-6-2γ membrane. Depending on the R^2 value presented in Table 3 and the results of the FRR%, the PPCA-6-2γ membrane was less prone to oil molecules accumulating after using the membrane for one time. This is because the formation of a hydration layer on the membrane surface at a low contact angle inhibited the retention of oil molecules. Therefore, during the washing process, the PPCA-6-2γ membrane's surface reduced the accumulated oil molecules because it has a low contact angle.

Figure 11 and Figure 12 show that the cake layer formation model was the best model for describing PPCA-6-2γ membrane fouling with a high R^2 value. Then, the R^2 value notably increased from just above 0.93 for the third cycle. The PPCA-6-2γ membrane suffered from deposition of oil droplets on the membrane pores due to the adsorption mechanism. The flux declined with time, even though the thickness of the fouling layer did not increase with time. To gain the desired antifouling characteristics of membranes, physical methods like backwashing, water flushing, and ultrasonication should be utilized with chemical agents.

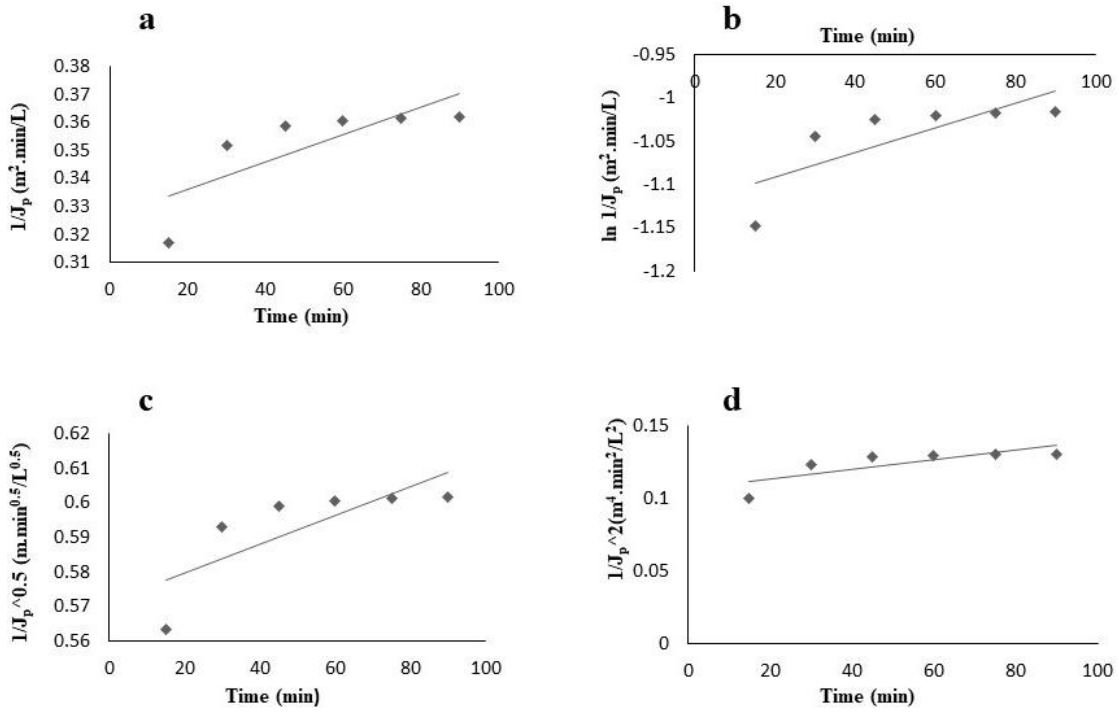

Figure 11: The linear plots of the fouling mechanism model for the first cycle of the PPCA-6-2γ membrane. a) intermediate pore blocking, b) complete pore blocking, c) standard pore blocking, and d) cake formation

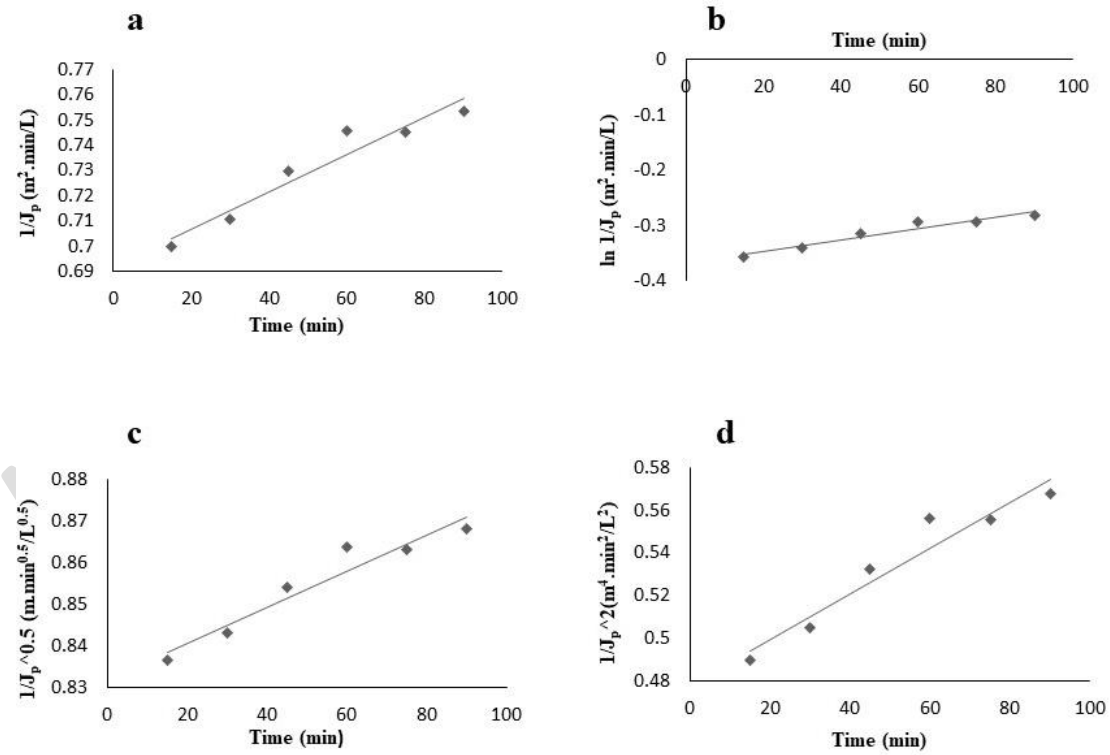

Figure 12: The linear plots of the fouling mechanism model for the third cycle of the PPCA-6-2γ membrane. a) intermediate pore blocking, b) complete pore blocking, c) standard pore blocking, and d) cake formation.

By applying the UF processes to oily water, the four models of fouling examined had a good linear correlation. This is an indication that all the fouling mechanisms are occurring simultaneously. For the PPCA-6-2 membrane, in every washing process, some oil molecules cannot be physically removed since they are strongly bonded to the membrane surface or pores. Particles left behind after every cycle resulted in a drop in the permeate flux and decreased the difference between the two readings. Thus, the value of R^2 increased after every cleaning process. The results showed that the oil fouled the membrane by depositing a cake layer, whereas certain oil molecules were adsorbed, immobilized on the surface, and imbibed into the membrane. Therefore, the permeate flux decreased each time the membranes were reused in the filtration processes.

Table 3: The fitting parameters of the first and third cycles of the PPCA-6-2γ membrane.

Membrane	Cycles	Intermediate pore blocking	Complete pore blocking	Standard pore blocking	Cake formation
PPCA-6-2γ membrane	First	y = 0.0005x + 0.3266 R^2 = 0.6091	y = 0.0014x - 1.1197 R^2 = 0.6001	y = 0.0004x + 0.5714 R^2 = 0.6046	y = 0.0003x + 0.1068 R^2 = 0.6183
	Third	y = 0.0007x + 0.6922 R^2 = 0.9290	y = 0.001x - 0.3671 R^2 = 0.9267	y = 0.0004x + 0.8321 R^2 = 0.9279	y = 0.0011x + 0.4782 R^2 = 0.9312

3.11. The costs of membrane manufacturing

The cost of total manufacturing of the MMMs will be determined according to Equation 13 and Equation 14, considering that the official price of power in Iraq for government institutions is 120 IQD/kWh, which is equivalent to 0.09091 $/kWh. Also, the price of the materials used in the membrane manufacturing was set as sold in the local stores (Saleem et al., 2025).

$$C_t = C_m + C_p \quad (13)$$

$$C_p = P_i * C_{op} \quad (14)$$

Where C_t is the cost of total manufacturing ($), C_m is the cost of total materials ($), C_p is the cost of total consumed electrical power ($), P_i is the power of instruments used in the manufacturing of the membrane (kWh), and C_{op} is the official price of power ($/kWh). The total cost of the consumed electrical power involved the power which is consumed in the casting solution preparation processes (sonication and stirring) and the casting process (film applicator machine).

Determination of manufacturing costs has been made per 20 g of the casting solution for the PPCA-6-2γ membrane according to the ratios shown in Table 1. This dose of a casting solution forms 0.1125 m^2 during casting by the casting machine. Table 4 presents the details of the material prices used in manufacturing the membrane. It shows that the total cost of the materials used in the manufacturing of the PPCA-6-2γ membrane was about 9.88 $, respectively. The total costs of the consumed electrical power were 1.67 $ as shown in Table 5. Table 6 shows the total manufacturing cost for the PPCA-6-2γ membrane. The manufacturing prices of the PPCA-6-2γ membrane have been compared with other pristine flat sheet UF membranes manufactured by Guochukeji Technology (Xiamen) Co., Ltd (China). As advertised by this company, the ex-price of these specified membranes is 180 $/$m^2$, but without the shipping cost. The shipping cost to Iraq is 100 $ by FedEx. So, the total price after shipping to Iraq becomes 280 $. The local manufacturing costs of the PPCA-6-2γ membranes did not surpass 90 $/$m^2$ of the membrane.

Table 4: Prices of materials used in the manufacturing of the PPCA-6-2γ membrane.

Material	Quantity		Price	Used quantity price
	wt.%	g	$/g	$
PAN/PSF	17	3.4	1.515	5.151
DMF	76.5	15.3	0.074	1.1322
$C_{12}EO_{10}$	6	1.2	0.067	0.0804
γ-Al_2O_3	2	0.4	4.667	1.8668
Total Price (γ-Al_2O_3)				8.2082

Table 5: : Cost estimate of the power used in PPCS-6-0.5 and PPCA-6-2γ membranes preparation.

Devices	Time	Power			
	(h)	W	W	Wh	kWh
Ultrasonic (γ-Al_2O_3)	3	100-1000	500	1500	1.5
Magnetic Stirrer	37	450	450	16650	16.65
Casting Machine	0.5	50-500	370	185	0.185
Total power (Al_2O_3)					18.34

Table 6: Total cost of the prepared membrane.

Cost of the used material for the PPCA-6-2γ membrane	9.88 $
Total cost of the PPCA-6-2γ membrane	88 $/$m^2$

3.12. Comparison of the performance of membranes

Table 7 compares the efficacy of the PPCA-6-2γ membrane in this study with several modified membranes utilizing different nanoparticles reported in the literature for the separation of oil from wastewater systems. Table 7 presents several important membrane properties, including CA, flux, and FRR%. The PPCA-6-2γ membrane showed a superior oil rejection and a higher FRR% compared to the membranes reported in the literature. The PPCA-6-2γ membrane exhibited

permeate with oil content that meets the WHO permissible limit for oily water discharge (oil concentration < 5 mg/L).

Table 7: Performance of prepared PPCA-6-2γ membrane compared to other developed membranes studied in the rejection of oil from wastewater.

Polymer	Additive type	Oil type	Contact angle (°)	Flux ($L/m^2.h$)	FRR%	Rejection (%)	Ref.
PVDF	Triton X-100, TiO_2 (2 wt.%), and CuO (2 wt.%)	O/W emulsion	53	>1800	99.9	95	(Rosset et al., 2025)
PES	Isotropic PES	Heavy O/W	39	65 ($L/h.m^2.bar$)	98.2	59.5	(Abdel-Aty et al., 2020)
PES/CA	0.5 wt.% 4A zeolite	Kerosene	29	91.1	97.7	98.8	(Abbas and Al-Jubouri, 2024)
PAN/PSF	γ-Al_2O_3 (2 wt.%) $C_{12}EO_{10}$ (6 wt.%)	VGO	26.55	189.2	95.4%	97.15%	Current study

4. Conclusions

This study involved the development of PAN/PSF blend membranes by adding $C_{12}EO_{10}$ and α-Al_2O_3 NPs and γ-Al_2O_3 NPs, both with an average size of 20 nm, at different concentrations. The PAN/PSF blend membrane, which contained 6wt.% $C_{12}EO_{10}$ and 2 wt.% γ-Al_2O_3 NPs exhibited the highest values of both hydrophilicity and porosity. The FT-IR analysis indicates the existence of functional groups on the surface of the PPCA-6-2γ membrane, hence confirming the incorporation of γ-Al_2O_3 NPs into the membrane structure. Measurements of contact angle demonstrated that the hydrophilicity of the PPCA-6-2γ membrane was enhanced, resulting in a significant improvement in the permeate flux. The PPCA-6-2γ membrane exhibited the highest

permeate flux of 189.2 L/m²·h, favorable hydrophilicity with a contact angle of 26.55°, and the best VGO rejection with COD removal% of 97.15% at 150 mg/L. The integration of Al_2O_3 NPs improved the anti-fouling effectiveness. The PPCA-6-2γ membrane demonstrated the highest FRR% of 95.4%, compared to 77.5% for the PAN membrane, signifying improved resistance to VGO adhesion and superior self-cleaning capability. The reusability of the membranes was established by verifying their efficiency after four cycles of filtration. Also, the cake layer formation model successfully explained the fouling that occurred in the PPCA-6-2γ membrane. The manufacturing costs were estimated for the PPCA-6-2γ membrane to be $1.67/20 g, respectively. So, the local manufacturing costs of the PPCA-6-2γ membrane did not surpass 90 $/m^2 of the membrane. This study revealed the efficacy of Al_2O_3 NPs in enhancing the performance of PAN/PSF blend membranes containing 6 wt.% of $C_{12}EO_{10}$ for addressing oily water challenges. This method is essential for regulating the release of greasy wastewater and other dangerous contaminants into natural water bodies.

Conflict of Interests

The authors declare no conflict of interest.

Funding

Not applicable

Reference

Abbas, S. M., and Al-Jubouri, S. M. (2024). High performance and antifouling zeolite@ polyethersulfone/cellulose acetate asymmetric membrane for efficient separation of oily wastewater. *Journal of Environmental Chemical Engineering*, *12*(3), 112775.

Abbas, S. M., and Al-Jubouri, S. M. (2025). ZrO2 Nanoparticles Filler-Based Mixed Matrix Polyethersulfone/Cellulose Acetate Microfiltration Membrane for Oily Wastewater Separation. *Applied Science and Engineering Progress*, *18*(1), 7599.

Abdel-Aty, A. A. R., Aziz, Y. S. A., Ahmed, R. M. G., ElSherbiny, I. M. A., Panglisch, S., Ulbricht, M., and Khalil, A. S. G. (2020). High performance isotropic polyethersulfone membranes for heavy oil-in-water emulsion separation. *Separation and Purification Technology*, *253*, 117467.

Abdikheibari, S., Lei, W., Dumée, L. F., Milne, N., and Baskaran, K. (2018). Thin film nanocomposite nanofiltration membranes from amine functionalized-boron nitride/polypiperazine amide with enhanced flux and fouling resistance. *Journal of Materials Chemistry A*, *6*(25), 12066–12081.

Abdulameer, H. N., and Al-Jubouri, S. M. (2022). A comparison study for the performance of polyethersulfone ultrafiltration mixed matrix membranes in The removal of heavy metal ions from aqueous solutions. *Iraqi Journal of Chemical and Petroleum Engineering*, *23*(2), 19–25.

Abdulsalam, M., Che Man, H., Goh, P. S., Yunos, K. F., Zainal Abidin, Z., Isma MI, A., and Ismail, A. F. (2020). Permeability and antifouling augmentation of a hybrid PVDF-PEG membrane using nano-magnesium oxide as a powerful mediator for POME decolorization. *Polymers*, *12*(3), 549.

Abedi, M., Chenar, M. P., and Sadeghi, M. (2015). Surface modification of PAN hollow fiber membrane by chemical reaction. *Fibers and Polymers*, *16*, 788–793.

Adday, A. S., and Al-Jubouri, S. M. (2025). Developing a versatile visible-light-driven polyvinylidene fluoride/Ag2O@ CRA photocatalytic membrane for efficient treatment of organic pollutants-contained wastewater. *Journal of Water Process Engineering*, *73*, 107713.

Ahmed, D. M., Ashour, E., and Shalaby, M. (2024). Recent advanced techniques in oil/water treatment. *Journal of Advanced Engineering Trends*, *43*(1), 383–393.

Ahmedzeki, N. S., Abdullah, S. M., and Salman, R. H. (2009). Treatment of industrial waste

water using reverse osmosis technique. *Journal of Engineering*, *15*(4), 4356–4363.

Ai-lian, L., & Qing, C. (1995). Polyacrylonitrilic/polysulfone (PAN/PS) blend ultrafiltration (UF) membranes. *Desalination*, *101*(1), 51–56.

Al-Maliki, R. M., Alsalhy, Q. F., Al-Jubouri, S., AbdulRazak, A. A., Shehab, M. A., Németh, Z., Hernadi, K., & Majdi, H. S. (2023). Enhanced antifouling in flat-sheet polyphenylsulfone membranes incorporating graphene oxide–tungsten oxide for ultrafiltration applications. *Membranes*, *13*(3), 269.

Amirilargani, M., Sabetghadam, A., and Mohammadi, T. (2012). Polyethersulfone/polyacrylonitrile blend ultrafiltration membranes with different molecular weight of polyethylene glycol: preparation, morphology and antifouling properties. *Polymers for Advanced Technologies*, *23*(3), 398–407.

Ang, M. B. M. Y., Macni, C. R. M., Caparanga, A. R., Huang, S.-H., Tsai, H.-A., Lee, K.-R., and Lai, J.-Y. (2020). Mitigating the fouling of mixed-matrix cellulose acetate membranes for oil–water separation through modification with polydopamine particles. *Chemical Engineering Research and Design*, *159*, 195–204.

Ayaz, M., Muhammad, A., Younas, M., Khan, A. L., and Rezakazemi, M. (2019). Enhanced water flux by fabrication of polysulfone/alumina nanocomposite membrane for copper (II) removal. *Macromolecular Research*, *27*, 565–571.

Cerar, J., Jamnik, A., Szilágyi, I., and Tomšič, M. (2021). Solvation of nonionic poly (ethylene oxide) surfactant Brij 35 in organic and aqueous-organic solvents. *Journal of Colloid and Interface Science*, *594*, 150–159.

Cortés, H., Hernández-Parra, H., Bernal-Chávez, S. A., Del Prado-Audelo, M. L., Caballero-Florán, I. H., Borbolla-Jiménez, F. V, González-Torres, M., Magaña, J. J., and Leyva-Gómez, G. (2021). Non-ionic surfactants for stabilization of polymeric nanoparticles for biomedical uses. *Materials*, *14*(12), 3197.

Dasgupta, J., Chakraborty, S., Sikder, J., Kumar, R., Pal, D., Curcio, S., and Drioli, E. (2014). The effects of thermally stable titanium silicon oxide nanoparticles on structure and performance of cellulose acetate ultrafiltration membranes. *Separation and Purification*

Technology, *133*, 55–68.

De Rosset, A., Torres-Mendieta, R., Pasternak, G., and Yalcinkaya, F. (2025). Synergistic effects of natural biosurfactant and metal oxides modification on PVDF nanofiber filters for efficient microplastic and oil removal. *Process Safety and Environmental Protection*, *194*, 997–1009.

Etemadi, H., Afsharkia, S., Zinatloo-Ajabshir, S., and Shokri, E. (2021). Effect of alumina nanoparticles on the antifouling properties of polycarbonate-polyurethane blend ultrafiltration membrane for water treatment. *Polymer Engineering & Science*, *61*(9), 2364–2375.

Etemadi, H., Amirjangi, A., Ghasemian, N., and Shokri, E. (2020). Synthesis and characterization of polycarbonate/TiO2 ultrafiltration membranes: critical flux determination. *Chemical Engineering & Technology*, *43*(11), 2247–2258.

Etemadi, H., and Qazvini, H. (2021). Investigation of alumina nanoparticles role on the critical flux and performance of polyvinyl chloride membrane in a submerged membrane system for the removal of humic acid. *Polymer Bulletin*, *78*(5), 2645–2662.

Ghaemi, N. (2016). A new approach to copper ion removal from water by polymeric nanocomposite membrane embedded with γ-alumina nanoparticles. *Applied Surface Science*, *364*, 221–228.

Hosseini, S. M., Karami, F., Farahani, S. K., Bandehali, S., Shen, J., Bagheripour, E., and Seidypoor, A. (2020). Tailoring the separation performance and antifouling property of polyethersulfone based NF membrane by incorporating hydrophilic CuO nanoparticles. *Korean Journal of Chemical Engineering*, *37*, 866–874.

Hu, L., Pu, Z., Zhong, Y., Liu, L., Cheng, J., and Zhong, J. (2020). Effect of different carboxylic acid group contents on microstructure and properties of waterborne polyurethane dispersions. *Journal of Polymer Research*, *27*, 1–9.

Ibrahim, Y., Naddeo, V., Banat, F., and Hasan, S. W. (2020). Preparation of novel polyvinylidene fluoride (PVDF)-Tin (IV) oxide (SnO_2) ion exchange mixed matrix membranes for the removal of heavy metals from aqueous solutions. *Separation and*

Purification Technology, *250*, 117250.

Iritani, E., and Katagiri, N. (2016). Developments of blocking filtration model in membrane filtration. *KONA Powder and Particle Journal*, *33*, 179–202.

Isloor, A. M., Nayak, M. C., Prabhu, B., Ismail, N., Ismail, A. F., and Asiri, A. M. (2019). Novel polyphenylsulfone (PPSU)/nano tin oxide (SnO_2) mixed matrix ultrafiltration hollow fiber membranes: Fabrication, characterization and toxic dyes removal from aqueous solutions. *Reactive and Functional Polymers*, *139*, 170–180.

Jain, H., Dhupper, R., Shrivastava, A., and Kumari, M. (2023). Enhancing groundwater remediation efficiency through advanced membrane and nano-enabled processes: A comparative study. *Groundwater for Sustainable Development*, *23*, 100975.

Kang, G., and Cao, Y. (2014). Application and modification of poly (vinylidene fluoride)(PVDF) membranes–a review. *Journal of Membrane Science*, *463*, 145–165.

Karbol, M.S., and Al-Jubouri, S. M. (2025). Developing the polyacrylonitrile/polysulfone blended polymer membranes by a non-ionic surfactant for efficient oily water separation. *Journal of Water and Environmental Nanotechnology*.

Karimi, A., Khataee, A., Vatanpour, V., and Safarpour, M. (2020). The effect of different solvents on the morphology and performance of the ZIF-8 modified PVDF ultrafiltration membranes. *Separation and Purification Technology*, *253*, 117548.

Khader, E. H., Mohammed, T. J., Albayati, T. M., Rashid, K. T., Saady, N. M. C., and Zendehboudi, S. (2025). Green nanoparticles blending with polyacrylonitrile ultrafiltration membrane for antifouling oily wastewater treatment. *Separation and Purification Technology*, *353*, 128256.

Koutahzadeh, N., Esfahani, M. R., Bailey, F., Taylor, A., and Esfahani, A. R. (2018). Enhanced performance of polyhedral oligomeric silsesquioxanes/polysulfone nanocomposite membrane with improved permeability and antifouling properties for water treatment. *Journal of Environmental Chemical Engineering*, *6*(5), 5683–5692.

Liang, B., Jiang, Q., Tang, S., Li, S., and Chen, X. (2016). Porous polymer electrolytes with high ionic conductivity and good mechanical property for rechargeable batteries. *Journal of*

Power Sources, *307*, 320–328.

Mondal, R., Chakraborty, T., Yadav, D., Bellare, J., Saxena, S., and Shukla, S. (2024). Poly (vinylidene fluoride)/Nickel Oxide–Montmorillonite Mixed-Matrix Membranes for Oil Separation from Emulsified Oily Wastewater. *ACS Applied Nano Materials*, *7*(19), 22752–22765.

Nazemidashtarjandi, S., Mousavi, S. A., and Bastani, D. (2017). Preparation and characterization of polycarbonate/thermoplastic polyurethane blend membranes for wastewater filtration. *Journal of Water Process Engineering*, *16*, 170–182.

Ruhland, K., Frenzel, R., Horny, R., Nizamutdinova, A., van Wüllen, L., Moosburger-Will, J., and Horn, S. (2017). Investigation of the chemical changes during thermal treatment of polyacrylonitrile and 15N-labelled polyacrylonitrile by means of in-situ FTIR and 15N NMR spectroscopy. *Polymer Degradation and Stability*, *146*, 298–316.

Sadek, S. A., and Al-Jubouri, S. M. (2023). Structure and performance of polyvinylchloride microfiltration membranes improved by green silicon oxide nanoparticles for oil-in-water emulsion separation. *Materials Today Sustainability*, *24*(August), 100600. https://doi.org/10.1016/j.mtsust.2023.100600

Sadek, S. A., and Al-Jubouri, S. M. (2024). Highly efficient oil-in-water emulsion separation based on innovative stannic oxide/polyvinylchloride (SnO_2/PVC) microfiltration membranes. *Journal of Industrial and Engineering Chemistry*.

Sadek, S. A., Al-Jubouri, S. M., and Al-Batty, S. (2024). Investigating the Fouling Models of the Microfiltration Mixed Matrix Membranes-Based Oxide Nanoparticles Applied for Oil-in-Water Emulsion Separation. *Iraqi Journal of Chemical and Petroleum Engineering*, *25*(2), 1–16.

Saleem, A. G., and Al-Jubouri, S. M. (2024). Efficient separation of organic dyes using polyvinylidene fluoride/polyethylene glycol-tin oxide (PVDF/PEG-SnO_2) nanoparticles ultrafiltration membrane. *Applied Science and Engineering Progress*, *17*(4), 7523.

Saleem, A. G., Al-Jubouri, S. M., Al-Batty, S., and Hakami, M. W. (2025). Determination of controlling fouling mechanism using the Hermia models and estimation of the

manufacturing costs of the modified polyvinylidene fluoride-based ultrafiltration membranes. *Iraqi Journal of Chemical and Petroleum Engineering*, *26*(1), 67–76.

Saraswathi, M. S. S. A., Rana, D., Alwarappan, S., Gowrishankar, S., Vijayakumar, P., and Nagendran, A. (2019). Polydopamine layered poly (ether imide) ultrafiltration membranes tailored with silver nanoparticles designed for better permeability, selectivity and antifouling. *Journal of Industrial and Engineering Chemistry*, *76*, 141–149.

Tan, X., and Rodrigue, D. (2019). A review on porous polymeric membrane preparation. Part II: Production techniques with polyethylene, polydimethylsiloxane, polypropylene, polyimide, and polytetrafluoroethylene. *Polymers*, *11*(8), 1310.

Tan, Y. H., Goh, P. S., Ismail, A. F., Ng, B. C., and Lai, G. S. (2017). Decolourization of aerobically treated palm oil mill effluent (AT-POME) using polyvinylidene fluoride (PVDF) ultrafiltration membrane incorporated with coupled zinc-iron oxide nanoparticles. *Chemical Engineering Journal*, *308*, 359–369.

Vatanpour, V., Madaeni, S. S., Khataee, A. R., Salehi, E., Zinadini, S., and Monfared, H. A. (2012). TiO_2 embedded mixed matrix PES nanocomposite membranes: Influence of different sizes and types of nanoparticles on antifouling and performance. *Desalination*, *292*, 19–29.

Wahab, M. Y., Muchtar, S., Jeon, S., Fang, L., Rajabzadeh, S., Takagi, R., Arahman, N., Mulyati, S., Riza, M., and Matsuyama, H. (2019). Synergistic effects of organic and inorganic additives in preparation of composite poly (vinylidene fluoride) antifouling ultrafiltration membranes. *Journal of Applied Polymer Science*, *136*(27), 47737.

Wahab, M. Y., Muchtar, S., Mulyati, S., Riza, M., Arahman, N., and Baig, M. A. A. (2019). Improvement of the characteristic of polyethersulfone membrane by blending with brij of different molecular weights. *Rasayan J. Chem.*, *12*(3), 1135–1143.

Zhang, Z., An, Q., Ji, Y., Qian, J., and Gao, C. (2010). Effect of zero shear viscosity of the casting solution on the morphology and permeability of polysulfone membrane prepared via the phase-inversion process. *Desalination*, *260*(1–3), 43–50.

Zhao, L., Liu, M., Xu, Z., Wei, Y., Xu, M., and Jiang, B. (2015). Modification of polysulfone

hollow fiber ultrafiltration membranes using hyperbranched polyesters with different molecular weights. *Polymers for Advanced Technologies*, *26*(4), 353–361.

Zhao, X., Su, Y., Chen, W., Peng, J., and Jiang, Z. (2012). Grafting perfluoroalkyl groups onto polyacrylonitrile membrane surface for improved fouling release property. *Journal of Membrane Science*, *415*, 824–834.

Zhao, X., Zhang, H., and Wang, J. (2025). Ultra-high flux electrospun PAN/MWCNTs/SiO2 membranes for oil–water separation: development and characterization. *Iranian Polymer Journal*, 1–10.

Zinadini, S., Rostami, S., Vatanpour, V., and Jalilian, E. (2017). Preparation of antibiofouling polyethersulfone mixed matrix NF membrane using photocatalytic activity of ZnO/MWCNTs nanocomposite. *Journal of Membrane Science*, *529*, 133–141.